PHYSICAL REVIEW C **96**, 015201 (2017)

Direct photon elliptic flow at energies available at the BNL Relativistic Heavy Ion Collider and the CERN Large Hadron Collider

Young-Min Kim,[1] Chang-Hwan Lee,[1] Derek Teaney,[2] and Ismail Zahed[2]
[1]*Department of Physics, Pusan National University, Busan 46241, Republic of Korea*
[2]*Department of Physics and Astronomy, Stony Brook University, New York 11794, USA*

(Received 22 October 2016; revised manuscript received 23 May 2017; published 17 July 2017)

We use an event-by-event hydrodynamical description of the heavy-ion collision process with Glauber initial conditions to calculate the thermal emission of photons. The photon rates in the hadronic phase follow from a spectral function approach and a density expansion, while in the partonic phase they follow from the Arnold-Moore-Yaffe (AMY) perturbative rates. The calculated photon elliptic flows are lower than those reported recently by both the ALICE and PHENIX collaborations.

DOI: 10.1103/PhysRevC.96.015201

I. INTRODUCTION

A chief finding of the heavy ion program both at the BNL Relativistic Heavy Ion Collider (RHIC) and CERN Large Hadron Collider (LHC) is a new state of matter under extreme conditions: the strongly coupled quark-gluon plasma (sQGP) [1–3]. The prompt release of a large entropy in the early partonic phase together with a rapid thermalization and short mean free paths suggest a nearly perfect fluid with a shear viscosity almost at its quantum bound. The time evolution of the fluid follows the laws of relativistic hydrodynamics. Detailed analyses of the hadronic spectra, including their q_T distributions and azimuthal anisotropies, have put some reliable constraints on the main characteristics of the relativistic viscous fluid, namely its shear viscosity.

The electromagnetic emissions in relativistic heavy ion collisions are thermal at low and intermediate q_T [4–6]. They are dominated by perturbative processes at high q_T. Since the photons interact very weakly on their way out, they are ideal for a better understanding of the hadronic composition, evolution, and spatial anisotropies of this fluid. They provide additional constraints on our understanding of the sQGP. Detailed analyses of the photon emissivities from both the partonic and hadronic phases, have led to some understanding of the overall photon yield at low and intermediate mass [2]. It is the purpose of this paper to extend these analyses and results to the recently reported anisotropies at both colliders [7–13].

To follow the evolution of the fluid, we will use an improved hydrodynamical model developed by one of us [14]. On an event-by-event basis, the model is initialized using the Glauber model, and its parameters are constrained by the measured charged multiplicities for fixed centralities [7,10,12,15,16]. The model yields reasonable event-by-event hadronic elliptic flows in semicentral collisions at both collider energies. We will use it to critically examine the photon anisotropies emanating from the partonic and hadronic composition of this hydrodynamical model.

Our analysis complements a number of recent theoretical studies of these anisotropies [5,6,17], although the analysis is, to a certain extent, less complete. Relative to other works, one of the major differences is the hadronic photon production rate, which was revisited by two of the authors [4]. We have not included the first viscous correction when computing the hadronic or partonic photon production rates. These corrections should ultimately be included in our computation. Nevertheless, we believe that the current comparison to data is complete enough to be of considerable value. First, comparing fairly to data requires a sizable code base, involving event-by-event viscous hydrodynamics and tabulated rates. It is certainly a good idea for more than one group to undertake such calculations. Looking forward to the beam energy scan at the RHIC collider, the current calculation develops the computational machinery to compute both photons and dileptons at lower energies where the hadronic rates play an increasingly important role.

In Sec. II, we briefly review the physical content of both the hadronic and partonic rates to be used in this analysis. In Sec. III we define the various azimuthal moments of the photon emission rates both in transverse momentum and rapidity. In Sec. IV we briefly overview the hydrodynamical setup for the space-time evolution of the fireball using the Glauber model for initial conditions. In Sec. V, we summarize our fitting function for the prompt photons. In Sec. VI, we detail the results for the simulated elliptic flows for both the charged particles and direct photons at RHIC and LHC. Our final conclusions are summarized in Sec. VII.

II. ELECTROMAGNETIC RADIATION IN HOT QCD MATTER

A. Hadronic photon rates

Thermal electromagnetic emissions at low and intermediate mass and q_T are involved due to the many reaction processes involving hadrons and the strong character of their interactions. The only organizational principles are broken chiral symmetry and gauge invariance, both of which are difficult to assert in reaction processes with hadrons in general. If hadrons thermalize with the pions and nucleons as the only strongly stable constituents, then there is a way to systematically organize the electromagnetic emissivities by expanding them not in terms of processes but rather in terms of final hadronic states. The

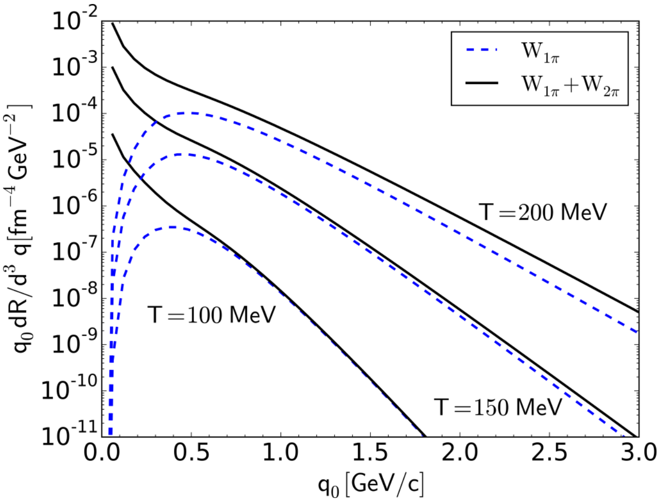

FIG. 1. Photon emission rates from $W_{1\pi}$ and $W_{2\pi}$ with $\mu_\pi = 0$ for $T = 100$, 150, and 200 MeV.

emissivities are then amenable to spectral functions by chiral reduction. These spectral functions are either tractable from other experiments or amenable to resonance saturation as we now briefly detail.

For a hadronic gas in thermal equilibrium the number of photons produced per unit four-volume and unit three-momentum can be related to the electromagnetic current-current correlation function [18]

$$\frac{q^0 dN_\gamma}{d^3q} = -\frac{\alpha_{\mathrm{em}}}{4\pi^2}\mathbf{W}(q), \tag{1}$$

with $q^2 = 0$ and

$$\mathbf{W}(q) = \int d^4x e^{-iqx}\mathrm{Tr}(e^{-(\mathbf{H}-F)/T}\mathbf{J}^\mu(x)\mathbf{J}_\mu(0)). \tag{2}$$

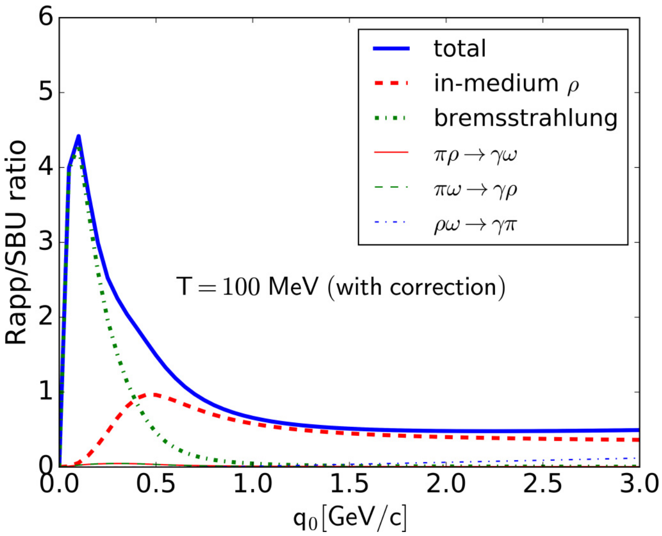

FIG. 2. Ratio of the thermal photon rates used in [26] (Rapp) to our corrected rates (SBU) for $T = 100$ MeV. Note that the prompt photon contribution is not included in the thermal photon rate.

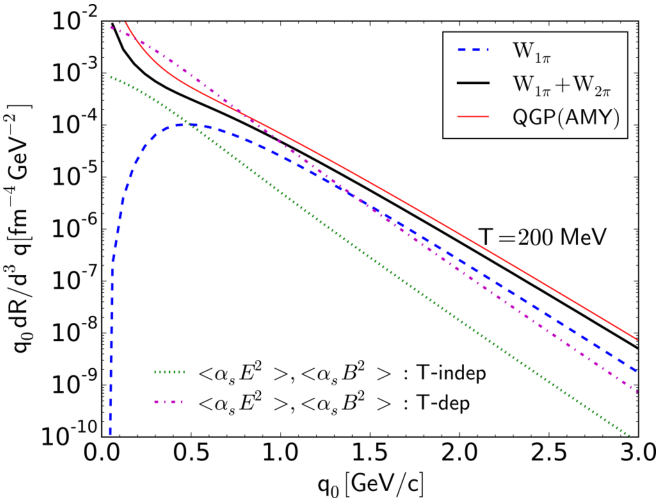

FIG. 3. Photon emission rates from $W_{1\pi}$ and $W_{2\pi}$ with $\mu_\pi = 0$ for $T = 200$ MeV are compared to the AMY rates (Arnold *et al.* [27] with $N_f = 3$) for $T = 200$ MeV. Also shown are the nonperturbative soft gluon corrections from [4,29].

In the above expression $\mathbf{J}_\mu$ is the hadronic part of the electromagnetic current, $\mathbf{H}$ is the hadronic Hamiltonian, and F is the free energy. The trace is over a complete set of stable hadronic states for temperatures below T_c, e.g., pions and nucleons. From the spectral representation and symmetry we can re-express the correlator in terms of the absorptive part of the time-ordered correlation function

$$\mathbf{W}(q) = \frac{2}{1+e^{q^0/T}}\,\mathrm{Im}\,i\int d^4x\, e^{iqx} \times \mathrm{Tr}(e^{-(\mathbf{H}-F)/T}T^*\mathbf{J}^\mu(x)\mathbf{J}_\mu(0)). \tag{3}$$

At RHIC and LHC the heat bath is net baryon free. The Feynman correlator in Eq. (3) can be expanded in terms of final pion states at finite temperature and zero baryon chemical potential

$$\mathbf{W}^F(q) = \mathbf{W}_{0\pi} + \int d\pi_1 \mathbf{W}_{1\pi} + \frac{1}{2!}\int d\pi_1 d\pi_2 \mathbf{W}_{2\pi} + \cdots, \tag{4}$$

with the pion thermal phase-space factors

$$d\pi_i = \frac{d^3k_i}{(2\pi)^3}\frac{n(E_i)}{2E_i}. \tag{5}$$

We have defined

$$\mathbf{W}_{n\pi} = i\int d^4x e^{iqx}\langle\pi^{a_1}(k_1)\cdots\pi^{a_n}(k_n)|T^*\mathbf{J}^\mu(x) \times \mathbf{J}_\mu(0)|\pi^{a_1}(k_1)\cdots\pi^{a_n}(k_n)\rangle, \tag{6}$$

with the sum over isospin subsumed. The first contribution in Eq. (4) vanishes for real photons since the heat bath is stable against spontaneous photon emission. The next two terms, $\mathbf{W}_{1\pi}$ and $\mathbf{W}_{2\pi}$, can be reduced to measurable vacuum

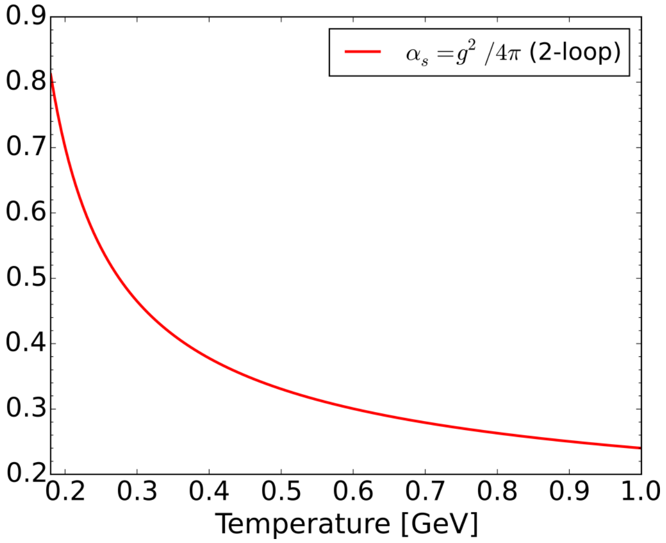

FIG. 4. Running strong coupling constant α_s up to two-loop order used in the AMY rates [31].

correlators [18], e.g.,

$$\begin{aligned}\mathbf{W}^F_{1\pi}(q,k) = {} & \frac{12}{f_\pi^2} q^2 \mathrm{Im}\,\Pi_V(q^2) \\ & - \frac{6}{f_\pi^2}(k+q)^2\,\mathrm{Im}\,\Pi_A((k+q)^2) + (q\to -q) \\ & + \frac{8}{f_\pi^2}\left[(kq)^2 - m_\pi^2 q^2\right]\mathrm{Im}\,\Pi_V(q^2) \\ & \times \mathrm{Re}\,\Delta_R(k+q) + (q\to -q),\end{aligned} \tag{7}$$

where ReΔ_R is the real part of the retarded pion propagator, and Π_V and Π_A are the transverse parts of the *VV* and *AA* correlators. Their spectral functions are related to both e^+e^- annihilation and τ-decay data as compiled in [19]. The two-pion reduced contribution $\mathbf{W}_{2\pi}$ is more involved. Its full unwinding can be found in [4,18,20–24].

In Fig. 1 we show the photon rates from the hadronic gas up to the two-pion contribution without pion chemical potential and with zero baryon chemical potential. The two-pion contribution $W_{2\pi}$ which includes $\pi\pi \to \rho\gamma$ and $\rho \to \pi\pi\gamma$ processes dominates at low q_0 as discussed in Dusling and Zahed [21]. Note that our two-pion results are reduced compared to their results due to a (corrected) reduced phase space in their numerical analysis. In Fig. 2 we compare the different rate contributions used by Rapp and collaborators [25] to our corrected rates at $T = 100$ MeV. Our corrected two-pion contribution which includes the bremsstrahlung is about three times smaller at the highest point near threshold. We note that in the diagrammatic analysis in [26] of the photon Bremsstrahlung, current conservation of the photon polarization function is enforced by hand, while in our analysis it is manifestly satisfied by the chiral reduction scheme.

B. QGP emission

There has been great progress in the calculation of the QGP photon rates in QCD both at leading [27] and next-to-leading orders [28]. We will not go over the details of the recent analyses but rather highlight the key points. First, the one-loop diagram corresponding to $q\overline{q} \to \gamma$ contributes at order α_s^0 for dileptons but vanishes at the photon point due to energy momentum conservation. One would then expect that the leading order in α_s contribution will come from two-loop diagrams corresponding to the annihilation $q + \overline{q} \to \gamma$ and Compton $g + q(\overline{q}) \to q(\overline{q}) + \gamma$ processes. However, these rates are plagued with collinear singularities [27]. Instead, a complete leading-order photon emission requires the inclusion of collinear bremsstrahlung and inelastic pair annihilations and their subsequent suppression through the Landau-Pomeranchuk-Migdal (LPM) effect [27]. We will refer to the next-to-leading order (NLO) QCD calculation as the resummed QGP Arnold-Moore-Yaffe (AMY) rates [27].

In Fig. 3, the resummed QGP (AMY) rates at high temperature [27] are compared to the hadronic rates at $T =$ 200 MeV. In Fig. 4, we summarize the running strong coupling constant α_s as a function of temperature used in assessing the AMY rates. The comparison shows that the AMY rates are substantially higher due to the running up of the coupling constant, an indication of nonperturbative physics as suggested in [4,29] and in [30]. Nonperturbative contributions through soft gluon insertions from [4,29] using the one-pion exchange expansion in leading order are also shown in Fig. 3 for comparison. We note that these contributions are substantial in the bremsstralung region. In contrast to the AMY rates, they are finite at zero photon frequency to guarantee a finite electric conductivity [4]. In the hydrodynamical estimates of the emissivities, only the hadronic and AMY rates will be retained. It is worth noting that the AMY rates used in the photon emissivities by the McGill group [5] make use of a fixed $\alpha_s \approx 0.3$ and are therefore lower than the ones we used with a running α_s as in Fig. 4.

TABLE I. PHENIX: Number of particles and simulation parameters for v_2 calculation in Figs. 8 and 9. The experimental data are taken from PHENIX [7,15]. N_{part} is the number of participants (nucleons) and N_{coll} is the number of collisions among nucleons. The centrality is mainly determined by N_{part}. The number of produced charged particles ($N_{\pi^\pm}$ and $N_{p+\bar{p}}$) in our simulations are much smaller than those in the experiments because our simulations were done only up to the freeze-out temperature.

	Simulation				Experiment			
Run ID	b (fm)	N_{part}	N_{coll}	$N_{\pi^\pm}$ (direct)	N_{part}	N_{coll}	$N_{\pi^\pm}$ (all)	Centrality
RHIC1	6.08 ± 0.01	214.67 ± 14.71	517.66 ± 59.73	149.73 ± 11.54	215.3 ± 5.3	532.7 ± 52.1	341.2 ± 30.0	15–20%
RHIC2	8.65 ± 0.01	114.43 ± 13.86	213.62 ± 40.17	73.00 ± 9.76	114.2 ± 4.4	219.8 ± 22.6	171.4 ± 16.6	30–40%
RHIC3	9.85 ± 0.01	74.52 ± 13.19	115.75 ± 30.30	44.92 ± 8.67	74.4 ± 3.8	120.3 ± 13.7	107.8 ± 10.8	40–50%

TABLE II. ALICE/CMS: Number of particles and parameters for the simulations including higher centrality as summarized in Figs. 10 and 11. The experimental data are taken from the ALICE and CMS experiments [10,12,16]. N_{part} is the number of participants (nucleons) and N_{coll} is the number of collisions among nucleons. The centrality is mainly determined by N_{part}. The produced charged particles ($N_{\pi^\pm}$ and $N_{p+\bar{p}}$) in our simulations are smaller than those in the experiments because our simulations were done only up to the freeze-out temperature.

	Simulation				Experiment			
Run ID	b (fm)	N_{part}	N_{coll}	$N_{\pi^\pm}$ (direct)	N_{part}	N_{coll}	$N_{\pi^\pm}$ (all)	Centrality
LHC1	4.27 ± 0.01	330.00 ± 12.24	1315.33 ± 104.34	549.27 ± 26.62	329 ± 3		1210 ± 84	5–10%
LHC2	6.49 ± 0.01	239.58 ± 16.12	811.27 ± 96.10	369.67 ± 29.62	240 ± 3			15–20%
LHC3	8.13 ± 0.01	170.28 ± 16.16	493.37 ± 79.87	246.09 ± 27.74	171 ± 3			25–30%
LHC4	9.49 ± 0.01	117.34 ± 15.79	278.78 ± 53.28	157.31 ± 22.75	118 ± 3			35–40%

The lattice EOS [32] includes a rapid crossover followed by an interpolation into the hadronic resonance gas phase. Even though there is no true phase transition, we choose $T_{\text{crit}} = 190$ MeV to allow a switch from partonic to hadronic electromagnetic emission. This choice of T_{crit} does not affect the hydrodynamic evolution.

III. AZIMUTHAL ANISOTROPY

The distribution of the emitted photons follow from the integrated space-time hydrodynamically evolved emission rates within the freeze-out volume

$$\begin{aligned}&\frac{d^3N_\gamma}{q_T dq_T dy d\phi}(q_T,y,\phi)\\&\quad= \int_{\tau_0}^{\tau_{f,o}} \tau d\tau \int_{-\infty}^{\infty} d\eta \int_0^{r_{\max}} r dr \int_0^{2\pi} d\theta\\&\qquad \times \left[q^0 \frac{dR_\gamma}{d^3q}(q = \vec{q}\cdot\vec{u}; T,\mu_B,\mu_\pi) \right] \Theta(T > T_{\text{FO}}). \qquad (8)\end{aligned}$$

Here $R_\gamma \equiv dN_\gamma/d^4x$ is the photon production rate, i.e., the number of direct photons per unit four-volume in the local rest frame of the fire ball. The hydrodynamical evolution is based on a numerical code developed by one of us [14]. Its key parameters will be briefly detailed in the next section. The rapidity is $y = \frac{1}{2}\ln[(E+q_L)/(E-q_L)]$, the proper time is $\tau = \sqrt{t^2 - z^2}$, and the spatial rapidity is $\eta = \frac{1}{2}\ln[(t+z)(t-z)]$ [33].

The elliptic flow and higher harmonics $v_n(q_T,y)$ in each event follow by expanding Eq. (8) in Fourier components. In general the Fourier series requires sines and cosines, or amplitudes and phases,

$$\begin{aligned}\frac{d^3N_\gamma}{q_T dq_T dy d\phi} &= \frac{1}{2\pi}\frac{d^2N_\gamma}{q_T dq_T dy}\\&\quad \times \left(1 + \sum_{n=1}^{\infty} v_{n\gamma}(q_T,y) e^{in[\phi - \Psi_{n\gamma}(q_T,y)]}\right) + \text{c.c.},\end{aligned} \qquad (9)$$

where c.c. denotes complex conjugation. The amplitude $v_{n\gamma}(q_T,y)$ is real and positive semidefinite, and the phase is real. The amplitudes and phases of the photon yield are combined into a single complex event-by-event flow coefficient

$$\mathcal{V}_{n\gamma}(q_T,y) \equiv v_{n\gamma}(q_T,y)e^{-in\Psi_{n\gamma}(q_T,y)}. \qquad (10)$$

The integrated event-by-event pion yield is also expanded in a Fourier series[1]

$$\frac{dN_\pi}{d\phi} = \frac{1}{2\pi}N_\pi\left(1 + \sum_{n=1}^{\infty} v_{n\pi}e^{in(\phi - \Psi_{n\pi})}\right) + \text{c.c.}, \qquad (11)$$

and the complex flow coefficients $\mathcal{V}_{n\pi} = v_{n\pi}e^{-in\Psi_{n\pi}}$ are defined in analogy with Eq. (10). The measured "photon elliptic flow" is the event-averaged correlation between the photon yield and integrated charged hadron yields which define the nth-order reaction plane. We will use the thermal pion yield as a proxy for this event plane, and therefore the photon elliptic flow is defined in the simulation as

$$v_{2\gamma}\{2\}(q_T,y) \equiv \frac{\langle \mathcal{V}_{n\gamma}(q_T,y)\mathcal{V}_{n\pi}^*\rangle}{\sqrt{\langle|\mathcal{V}_{n\pi}|^2\rangle}}, \qquad (12)$$

where the bracket refers to event averaging. We will use this operational definition of the photon elliptic flow in what follows.

IV. BRIEF ON HYDRODYNAMICS

The collision region is modeled using a relativistic hydrodynamic simulation tuned to reproduce hadronic observables. In this section we briefly discuss the model, including the initial conditions and equation of state (EOS), but leave the technical details to the literature [14]. We use the PHOBOS Glauber Monte Carlo [34] model to initialize the entropy density $s(\tau_o,\boldsymbol{x})$ in the transverse plane at an initial proper time τ_o according to a two-component model. Briefly, for the ith participant we assign a weight

$$A_i \equiv \kappa\left[\frac{(1-\alpha)}{2} + \frac{\alpha}{2}(n_{\text{coll}})_i\right], \qquad (13)$$

where $\alpha = 0.11$ is adjusted to reproduce the mean multiplicity versus centrality. At the LHC we take $\kappa = 27.0$, while at the RHIC we take $\kappa = 15.5$ so that $\kappa_{\text{LHC}}/\kappa_{\text{RHIC}} = 1.74$ which matches the ratio of multiplicities at the two colliding systems. $(n_{\text{coll}})_i$ is the number of binary collisions experienced by the ith participant. The entropy density in the transverse plane at

---

[1] The event-by-event pions yield a contribution of direct pions and feed-down pions from resonance decays. We will work with the direct-pion yield in what follows.

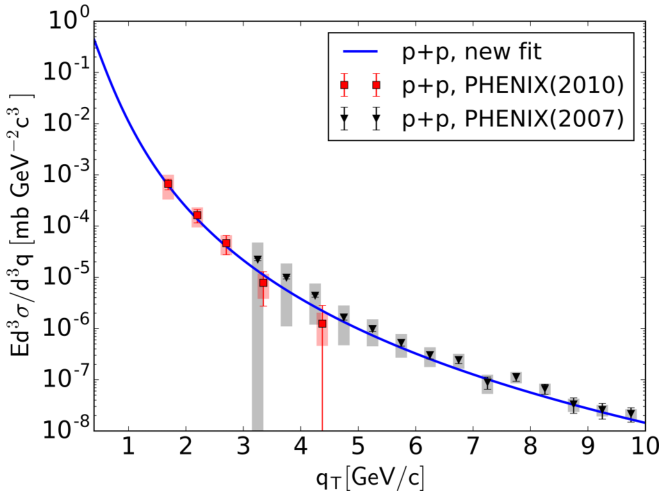

FIG. 5. Prompt-photon spectra fitted to PHENIX $p+p$ data [37,38].

initial time τ_o and transverse position $\boldsymbol{x} = (x,y)$ is taken to be

$$s(\tau_o,\boldsymbol{x}) = \sum_{i\,\text{parts}} s_i(\tau_o,\boldsymbol{x}-\boldsymbol{x}_i), \tag{14}$$

where $\boldsymbol{x}_i = (x,y)$ labels the transverse coordinates of the ith participant, and

$$s_i(\tau_o,\boldsymbol{x}) = A_i \frac{1}{\tau_o(2\pi\sigma^2)} e^{-\frac{x^2}{2\sigma^2}-\frac{y^2}{2\sigma^2}}, \tag{15}$$

with $\sqrt{2}\sigma = 0.7$ fm. The parameters κ and α are comparable to those used in [35].

Table I shows the choice of parameters [7,15] for PHENIX (^{197}Au+Au at $\sqrt{s_{NN}} = 200$ GeV). Again, N_{part} is the number of participants (nucleons) and N_{coll} is the number of collisions among nucleons. The nucleon-nucleon inelastic cross section is $\sigma_{\text{inel}}^{NN} = 40$ mb [36], and the entropy per wounded nucleon is $S_{\text{WN}} = 15.5$. Table II shows the choice of parameters [10,12,16] for ALICE and CMS (^{208}Pb+Pb at $\sqrt{s_{NN}} = 2.76$ TeV). The inelastic nucleon-nucleon cross section is $\sigma_{\text{inel}}^{NN} = 64$ mb [13], and the entropy per wounded nucleon is now $S_{\text{WN}} = 27$. In order to take into account the event-by-event fluctuations, we performed 300 runs for each centrality region. For PHENIX data the freeze-out temperature is set to $T_{\text{FO}} = 137$ MeV, while for ALICE data the freeze-out temperature is set slightly lower with $T_{\text{FO}} = 131$ MeV.

V. PHOTON SPECTRA

The direct photons include thermal photons as well as prompt photons which are produced by hard parton-parton collisions and can be assumed azimuthally symmetric. The prompt-photon spectrum can be estimated by an empirical model to fit the measured-photon spectrum in $p+p$ collisions scaled by the number of binary collisions. The empirical model is described in [17,40] (and references therein) as

$$q_0\frac{d^3N_\gamma^{\text{prompt}}}{d^3q} = q_0\frac{d^3\sigma^{pp}}{d^3q}\frac{N_{\text{coll}}}{\sigma_{NN}^{\text{inel}}}, \tag{16}$$

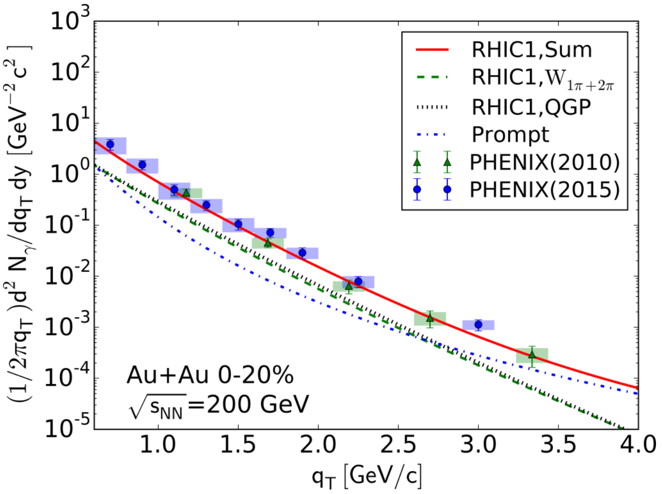

(a) 0-20%

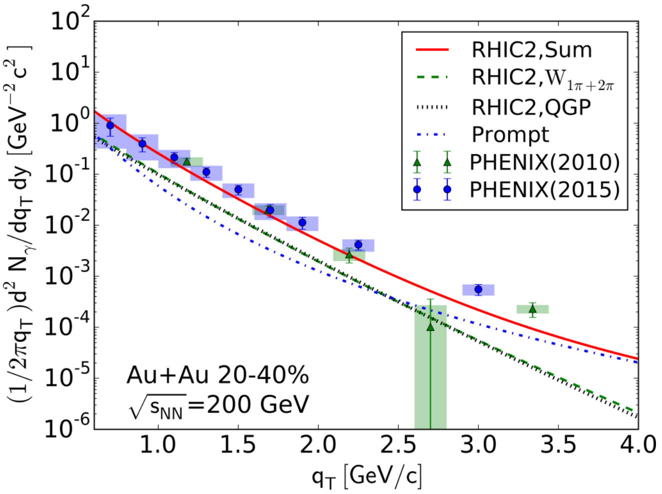

(b) 20-40%

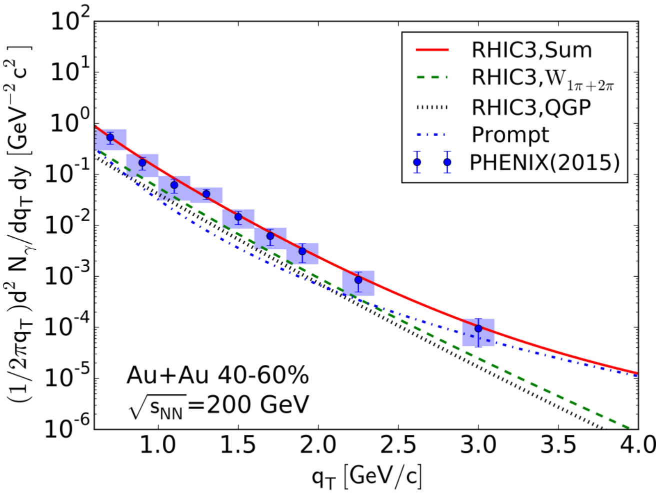

(c) 40-60%

FIG. 6. Spectra of direct photons for RHIC. Experimental data for PHENIX Au + Au are taken from [38,39]. See text.

where N_{coll} is the number of nucleon-nucleon (NN) collisions and $\sigma_{NN}^{\text{inel}}$ is the inelastic scattering cross section in NN

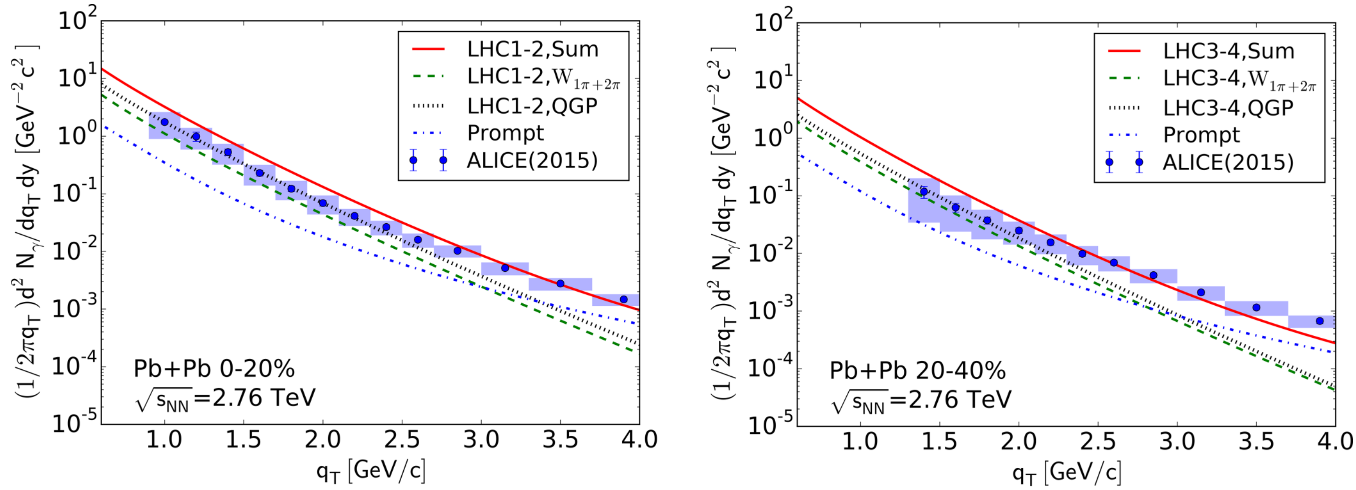

(a) 0-20%

(b) 20-40%

FIG. 7. Spectra of direct photon for ALICE. Experimental data for ALICE Pb + Pb are taken from [41]. Note that LHC1-2 (LHC3-4) was averaged over two centrality ranges, 0–10% and 10–20% (20–30% and 30–40%), weighted by the number of photons at each centrality bin [44]. See text.

collisions. To parametrize the prompt photon at RHIC for $p + p$ collisions, we will use the parametrization [38]

$$q_0 \frac{d^3\sigma^{pp}}{d^3q} = A\left(1+\frac{q_T^2}{B}\right)^{-n} \frac{\text{mb}}{\text{GeV}^2 c^{-3}}. \qquad (17)$$

The parameters $A = 2.6955$, $B = 0.19943$ and $n = 3.0631$ follow by fitting the $p + p$ spectrum in the PHENIX experiment [37,38] as shown in Fig. 5.

In Fig. 6 we show our direct-photon spectrum in comparison to the PHENIX (^{197}Au + ^{197}Au at $\sqrt{s_{NN}} = 200$ GeV) [38,39] measurements. The blue dot-dashed lines correspond to the prompt-photon spectrum which is obtained from the $p + p$ spectra in Fig. 5 scaled by the number of binary collisions. The dashed and dotted lines correspond to our predictions of the thermal photon production for hadronic and QGP contributions. The red solid line is the total spectrum of the direct photons which is obtained by summing the thermal and prompt photons.

The prompt $p + p$ spectrum has not been reported by ALICE [41]. However, a theoretical analysis of the PHENIX data using perturbative QCD at NLO shows a strong sensitivity to $\sqrt{s}$ in extrapolating the prompt spectra from RHIC to LHC [42,43]. The p_T dependence of the prompt spectrum at $\sqrt{s} =$ 2.76 TeV in [42,43] can be reproduced by the parametrization (17) with the parameter set $A = 0.55269$, $B = 0.48304$, and $n = 2.6788$. It is substantially higher than the one reported by PHENIX in the same p_T range. In Fig. 7 we show our direct-photon spectrum in comparison to ALICE (^{208}Pb + ^{208}Pb at $\sqrt{s_{NN}} = 2.76$ TeV) measurements [41]. The description of the curves is identical to the one presented for PHENIX above. We note that the prompt yield following from Eq. (17) becomes comparable to our hadronic yield at small p_T. Overall, our direct-photon yields are larger than those reported recently by the McGill group for the same p_T ranges and centralities [5]. This is most likely due to our use of the running coupling constant in the AMY rates which is larger.

VI. NUMERICAL RESULTS

A. Elliptic flow at RHIC

In Fig. 8, the simulation results for PHENIX v_2 of charged particles are summarized and compared with the experimental results [7,15,36]. The parameters used in our simulations are summarized in Table I. The nucleon-nucleon inelastic cross section $\sigma_{\text{inel}}^{NN} = 40.0$ mb is consistent with the referred cross section for the Glauber model, $\sigma_{\text{inel}}^{NN} = 42 \pm 3$ [36]. Note that the numbers of produced charged particles (N_π and N_p) in our simulations are smaller than those in experiments because our simulations were done only up to the freeze-out temperature. Resonance decays are not included. For PHENIX, our simulated elliptic flows of charged particles are somewhat below the experimental data in most of the ranges of the transverse momentum, especially at high transverse momentum. For low centrality, 0–20% in Fig. 8(a), our best-fit simulation results are consistent with the experimental results. For middle and high centralities in Figs. 8(b) and 8(c), the simulation results are below the experimental data.

In Fig. 9, the elliptic flow v_2 of direct photons for PHENIX are summarized [7–9,15,36]. The hadronic contributions are referred to as one-pion and two-pion following from the chiral reduction formulas Eq. (4). The solid lines are the full simulation results from T_{init} to T_{FO}. The dashed and dotted lines are the results with partial contribution from the hadrons below T_{crit} and the AMY resummed QGP above T_{crit}. The centrality ranges shown below the figures are based on the experimental data. In Fig. 9, we see that the difference between the one-pion (red) and two-pion (blue) contributions to the flow are not significant. Since the prompt yield following from Eq. (17) becomes comparable to our hadronic yield at small p_T, it adds to the depletion of the photon flow in this range. Overall, our

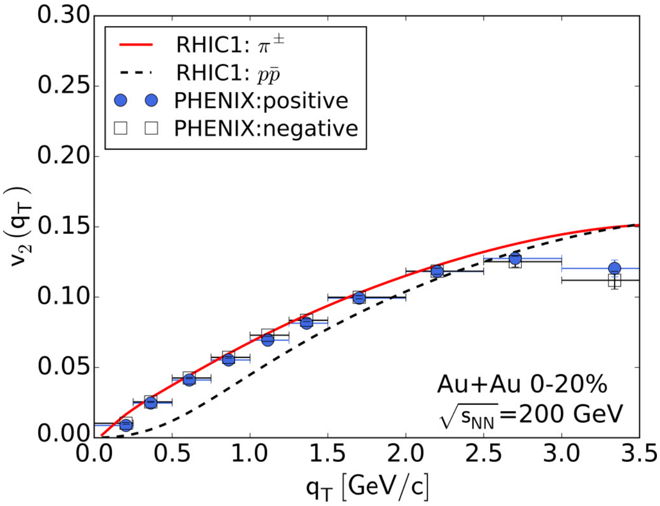

(a) 0-20% centrality

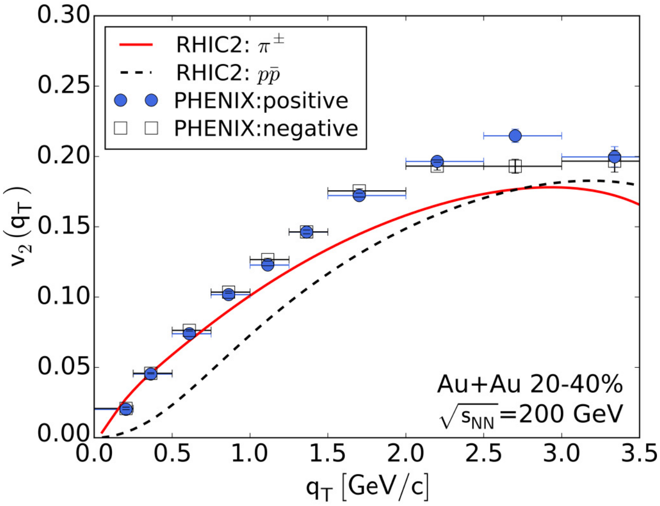

(b) 20-40% centrality

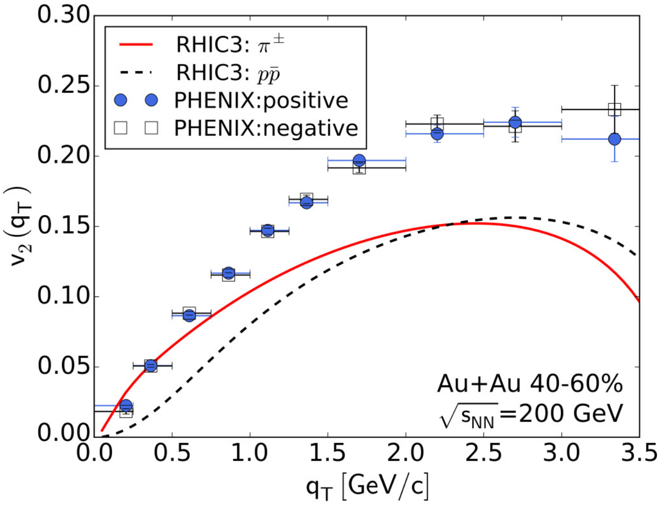

(c) 40-60% centrality

FIG. 8. Elliptic flow v_2 of charged particles ($\pi^{\pm},p,\bar{p}$) for PHENIX [7]. Simulation parameters are summarized in Table I. Best-fit results in a given centrality region are displayed.

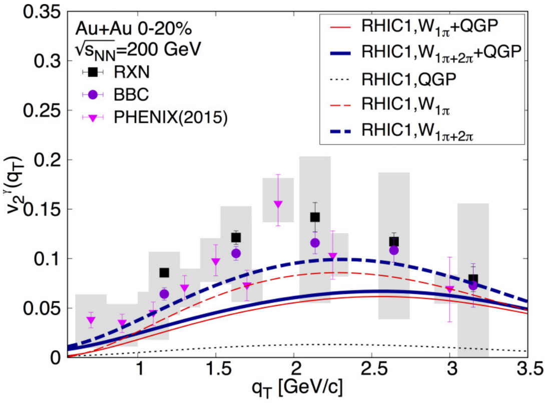

(a) 0-20% centrality

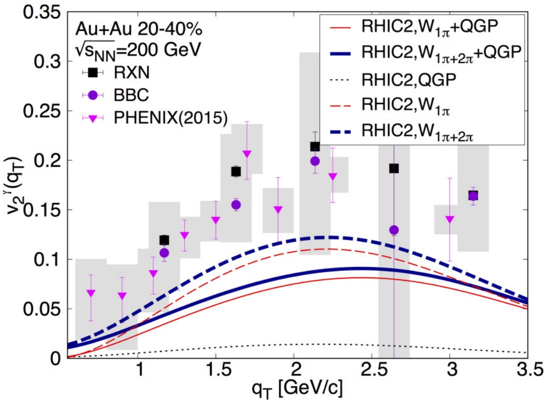

(b) 20-40% centrality

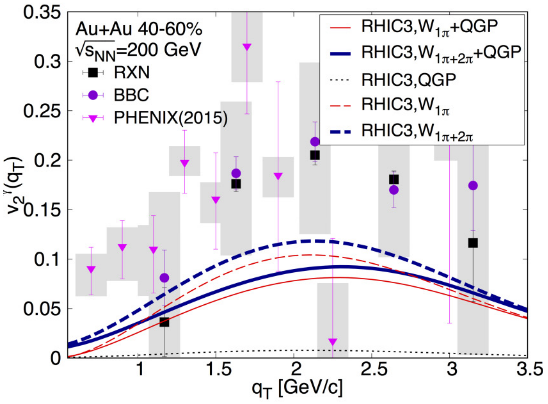

(c) 40-60% centrality

FIG. 9. Direct-photon elliptic flow v_2^{γ} for PHENIX [8,9]. For the hadronic part before the phase transition, first-order (CRF1 in red; up to one-pion contribution) and second-order (CRF2 in blue; up to two-pion contribution) hadronic resonance gas (HRG) models are used. In this calculation, T_{crit} is 190 MeV and T_{FO} is 137.44 MeV. The solid lines are full simulation results from T_{init} to T_{FO} with the phase transition from QGP to HRG. The dashed and dotted lines are the results with partial contributions from the HRG (below T_{crit}) and the QGP (above T_{crit}), respectively. The vertical error bars on each data point indicate the statistical uncertainties and the grey shaded regions indicate the systematic uncertainties of the experiment. RXN correspond to the data from a dedicated reaction-plane detector (RXN) of PHENIX [8]. BBC correspond to the data from beam-beam counters (BBC) of PHENIX [8].

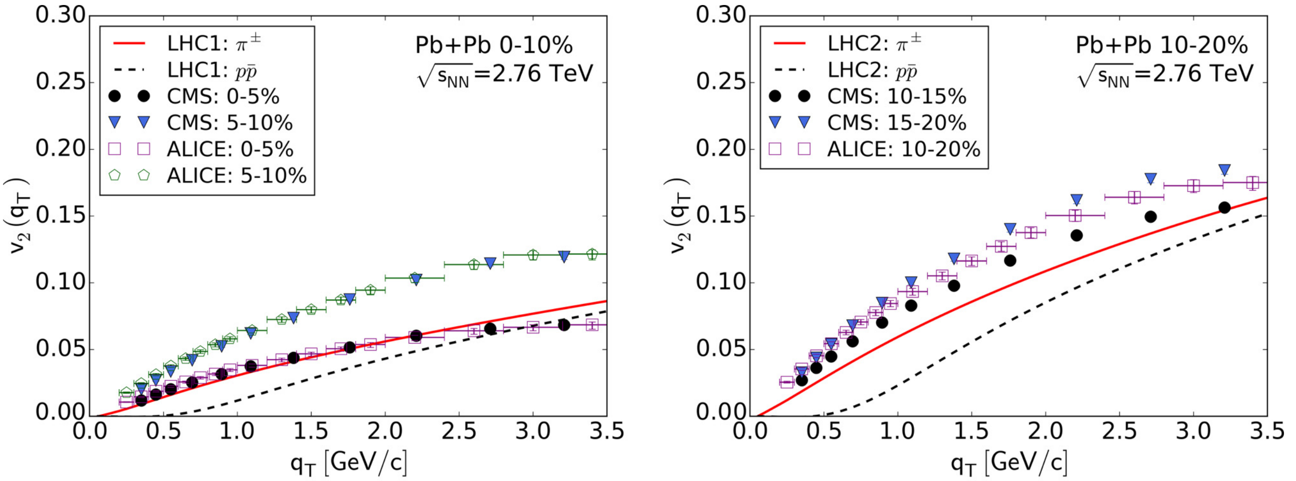

(a) 0-10% centrality (b) 10-20% centrality

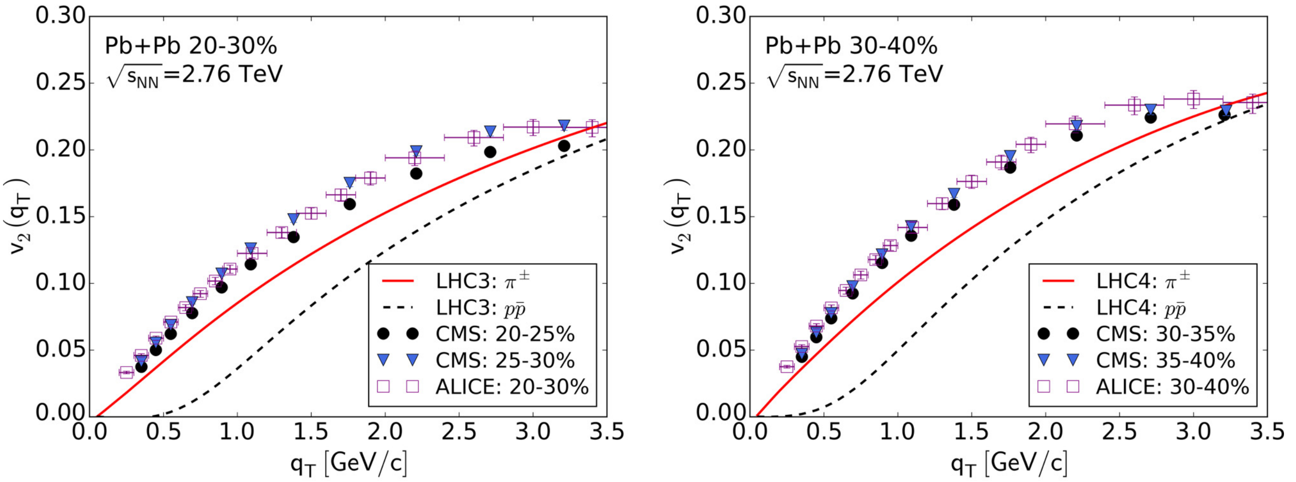

(c) 20-30% centrality (d) 30-40% centrality

FIG. 10. Elliptic flow v_2 of charged particles ($\pi^\pm, p, \bar{p}$) for ALICE and CMS [10,12]. Simulation parameters are summarized in Table II. Best-fit results in a given centrality region are shown.

elliptic flow for the photons is lower than the one reported by PHENIX [7–9,15,36].

B. Elliptic flow at LHC

In this section, we summarize our best-fit simulation results for the photon elliptic flow for ALICE and CMS data (^{208}Pb+Pb at $\sqrt{s_{NN}} = 2.76$ TeV). In Fig. 10, the simulation results for ALICE/CMS v_2 of charged particles are summarized and compared with the experimental results [10,12,13,16,45]. The parameters used in our simulations are summarized in Table II. We used the nucleon-nucleon inelastic cross section $\sigma_{\text{inel}}^{NN} = 64.0$ mb, which is consistent with the referred cross section for the Glauber model, $\sigma_{\text{inel}}^{NN} = 64 \pm 5$ [13]. Note that the numbers of produced charged particles (N_π and N_p) in our simulations are smaller than those in experiments because our simulations do not account for resonance decays. The simulated elliptic flows of charged particles for ALICE and CMS are below the empirical values except for the low-centrality 0–5% experimental data. In Fig. 10, as the centrality increases, in general, the elliptic flow v_2 increases for both the simulation and experiment.

In Fig. 11, the elliptic flow v_2 of direct photons for ALICE data are summarized [10–13,16,45].[2] Before the phase change from partonic to hadronic, both first-order (up to one-pion contribution) and second-order (up to two-pion contribution) HRG models are used. The solid lines are the full simulation results from T_{init} to T_{FO}. The dashed and dotted lines are the results with partial contributions from the HRG below T_{crit} and the QGP above T_{crit}. Note that the centrality ranges of the experimental data are only 0–40% in all plots in Fig. 11. Overall, our photon v_2 is again smaller than the one reported by ALICE.

---

[2] Experimental data of direct photons for ALICE are digitized from Fig. 5 in [11] using a graph digitizer software, GRAPHCLICK (http://www.arizona-software.ch/graphclick/).

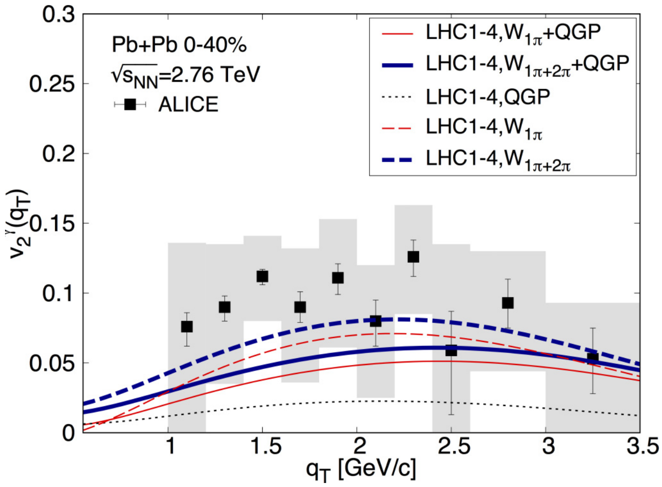

FIG. 11. Direct-photon elliptic flow v_2^γ for ALICE [11]. Before the phase transition, first-order HRG (CRF1 in re; up to one-pion contribution) and second-order HRG (CRF2 in blu; up to two-pion contribution) are used. T_{crit} is 190 MeV and T_{FO} is 131 MeV. T_{init} are summarized in Table II. The solid lines are full simulation results from T_{init} to T_{FO}. The dashed and dotted lines are the results with partial contributions from the HRG (below T_{crit}) and the QGP (above T_{crit}), respectively. Note that the centrality range of the experimental data are 0–40%. LHC1-4 is an average of our four predictions over four centrality ranges weighted by the number of photons at each centrality range [44]. The vertical error bars on each data point indicate the statistical uncertainties and the grey shaded regions indicate the systematic uncertainties of the experiment.

VII. CONCLUSIONS

We have assessed the elliptic flows of charged particles and direct photons at RHIC and LHC experiments using the recently revisited electromagnetic current-current correlators [4]. To determine the physical parameters of the hydrodynamic simulations for given centralities, we used the experimentally reported multiplicities of charged particles [7,10,12,15,16]. We have estimated the elliptic flow of charged particles and direct photons. For the electromagnetic radiation, we used the HRG rates for T_{crit} and the resummed AMY QGP rates above T_{crit}. For PHENIX, our simulated elliptic flows of charged particles are somewhat below the experimental data in most of the ranges of transverse momenta, especially at high transverse momentum as in Fig. 8.

In contrast, for ALICE and CMS, the simulated elliptic flows of charged particles are below the empirical values at low transverse momentum but reach the empirical values at high transverse momentum ~3.5 GeV/c as in Fig. 9. For the elliptic flow of direct photons, the situation is more subtle because the observed direct photons can be generated in both the HRG and the QGP phase. Overall, we found that our photon flows are lower than the ones reported by both the PHENIX and ALICE collaborations.

Our direct-photon yields are larger than those reported in [5] for the range of p_T and centralities discussed above, due in part to our larger AMY rates when using a running strong coupling α_s. However, our photon flows are somehow smaller. There are several reason for this: (1) our AMY rates are larger, which means more early photons with lower v_2; (2) our hadronic v_2 are slightly lower than those reported empirically, dragging our photon v_2; (3) our freeze-out temperature for the photons is higher than the one used in [5], to allow for extra photon emission from late-stage resonance decays.

Finally, we note that our photon rate calculations do not include the subtle effects of the viscous corrections as discussed in [46]. The chief reason is that our chiral reduction scheme is not reducible to specific diagrammatic contributions for which local distribution functions with viscous corrections can be implemented. How to implement the effects of viscosity in the chiral reduction scheme is an open problem. Because of this, we cannot reliably assess the contribution of these missing effects on our final results.

ACKNOWLEDGMENTS

We thank Kevin Dusling for discussions. We particularly thank Jean-Francois Paquet for making his prompt pp spectra available for comparison and for many discussions. The work of Y.M.K. and C.H.L. was supported by the National Research Foundation of Korea (NRF) grant funded by the Korea government (MSIP) (No. 2015R1A2A2A01004238 and No. 2016R1A5A1013277). The work of D.T. and I.Z. was supported in part by U.S. DOE Grant No. DE-FG02-88ER40388.

---

[1] U. Heinz and R. Snellings, Annu. Rev. Nucl. Part. Sci. **63**, 123 (2013).
[2] M. Luzum and H. Petersen, J. Phys. G **41**, 063102 (2014).
[3] D. A. Teaney, *Viscous Hydrodynamics and the Quark Gluon Plasma*, edited by R. C. Hwa and X.-N. Wang, Quark-Gluon Plasma 4 (World Scientific, 2010), pp. 207–266.
[4] C.-H. Lee and I. Zahed, Phys. Rev. C **90**, 025204 (2014).
[5] J. F. Paquet, C. Shen, G. S. Denicol, M. Luzum, B. Schenke, S. Jeon, and C. Gale, Phys. Rev. C **93**, 044906 (2016).
[6] H. v. Hees, C. Gale, and R. Rapp, Phys. Rev. C **84**, 054906 (2011); R. Rapp, H. v. Hees, and M. He, Nucl. Phys. A **931**, 696 (2014).
[7] S. S. Adler *et al.* (PHENIX Collaboration), Phys. Rev. Lett. **91**, 182301 (2003).
[8] A. Adare *et al.* (PHENIX Collaboration), Phys. Rev. Lett. **109**, 122302 (2012).
[9] A. Adare *et al.* (PHENIX Collaboration), Phys. Rev. C **94**, 064901 (2016).
[10] B. Abelev *et al.* (ALICE Collaboration), Phys. Lett. B **719**, 18 (2013).
[11] D. Lohner (ALICE Collaboration), J. Phys. Conf. Ser. **446**, 012028 (2013).
[12] S. Chatrchyan *et al.* (CMS Collaboration), Phys. Rev. C **87**, 014902 (2013).
[13] S. Chatrchyan *et al.* (CMS Collaboration), Phys. Rev. C **89**, 044906 (2011).
[14] A. Mazeliauskas and D. Teaney, Phys. Rev. C **91**, 044902 (2015).

[15] S. S. Adler *et al.* (PHENIX Collaboration), Phys. Rev. C **69**, 034909 (2004).

[16] B. Abelev *et al.* (ALICE Collaboration), Phys. Rev. C **88**, 044910 (2013).

[17] S. Turbide, R. Rapp, and C. Gale, Phys. Rev. C **69**, 014903 (2004).

[18] J. V. Steele, H. Yamagishi, and I. Zahed, Phys. Lett. B **384**, 255 (1996).

[19] Z. Huang, Phys. Lett. B **361**, 131 (1995).

[20] J. V. Steele, H. Yamagishi, and I. Zahed, Phys. Rev. D **56**, 5605 (1997).

[21] K. Dusling and I. Zahed, Phys. Rev. C **82**, 054909 (2010).

[22] C.-H. Lee, H. Yamagishi, and I. Zahed, Phys. Rev. C **58**, 2899 (1998).

[23] K. Dusling, D. Teaney, and I. Zahed, Phys. Rev. C **75**, 024908 (2007).

[24] K. Dusling and I. Zahed, Phys. Rev. C **80**, 014902 (2009).

[25] M. Heffernan, P. Hohler, and R. Rapp, Phys. Rev. C **91**, 027902 (2015).

[26] W. Liu and R. Rapp, Nucl. Phys. A **796**, 101 (2007).

[27] P. Arnold, G. D. Moore, and L. G. Yaffe, J. High Energy Phys. 11 (2000) 001; 12 (2001) 009; 05 (2003) 051.

[28] J. Ghiglieri, J. Hong, A. Kurkela, E. Lu, G. D. Moore, and D. Teaney, J. High Energy Phys. 05 (2013) 010.

[29] C. H. Lee, J. Wirstam, I. Zahed, and T. H. Hansson, Phys. Lett. B **448**, 168 (1999).

[30] C. Gale, Y. Hidaka, S. Jeon, S. Lin, J. F. Paquet, R. D. Pisarski, D. Satow, V. V. Skokov, and G. Vujanovic, Phys. Rev. Lett. **114**, 072301 (2015).

[31] K. G. Chetyrkin, B. A. Kniehl, and M. Steinhauser, Nucl. Phys. B **510**, 61 (1998).

[32] M. Laine and Y. Schröder, Phys. Rev. D **73**, 085009 (2006).

[33] J. D. Bjorken, Phys. Rev. D **27**, 140 (1983).

[34] B. Alver, M. Baker, C. Loizides, and P. Steinberg, arXiv:0805.4411.

[35] Z. Qiu, arXiv:1308.2182.

[36] S. S. Adler *et al.* (PHENIX Collaboration), Phys. Rev. Lett. **91**, 072301 (2003).

[37] S. S. Adler *et al.* (PHENIX Collaboration), Phys. Rev. Lett. **98**, 012002 (2007).

[38] A. Adare *et al.* (PHENIX Collaboration), Phys. Rev. Lett. **104**, 132301 (2010).

[39] A. Adare *et al.* (PHENIX Collaboration), Phys. Rev. C **91**, 064904 (2015).

[40] D. K. Srivastava, Eur. Phys. J. C **22**, 129 (2001).

[41] J. Adam *et al.* (ALICE Collaboration), Phys. Lett. B **754**, 235 (2016).

[42] P. Aurenche, J. P. Guillet, E. Pilon, M. Werlen, and M. Fontannaz, Phys. Rev. D **73**, 094007 (2006).

[43] J. F. Paquet, Ph.D. thesis, McGill University, 2015.

[44] D. Lohner, Ph.D. thesis, University of Heidelberg, 2013.

[45] S. Chatrchyan *et al.* (CMS Collaboration), Phys. Rev. C **84**, 024906 (2011).

[46] C. Shen, U. W. Heinz, J. F. Paquet, I. Kozlov, and C. Gale, Phys. Rev. C **91**, 024908 (2015); C. Shen, U. Heinz, J. F. Paquet, and C. Gale, Nucl. Phys. A **932**, 184 (2014); U. W. Heinz, J. Liu, and C. Shen, *ibid.* **932**, 310 (2014).